

RESEARCH

Open Access



Experimental Study on Existing RC Circular Members Under Unequal Lateral Impact Train Collision

Khalil AL-Bukhaiti^{1*} , Liu Yanhui^{1*}, Zhao Shichun¹, Hussein Abas¹, Xu Nan¹, Yang Lang¹, Yan Xing Yu¹ and Han Daguang²

Abstract

With the fast growth of high-speed rail in recent years, derailment has become the first hidden danger of high-speed rail transportation. The high-speed train passes near the station building. So the train may derail and hit the station building. Building a high-speed railway station usually uses a reinforced concrete structure. As a result of high impact energy on the impact body, the reinforced concrete (RC) member may fail; the impact point is near the member's foot; the structural member's constraint can be considered fixed support. This paper investigates the dynamic behavior of four types of circular reinforced concrete members under unequal lateral impact loads. The RC member's failure mechanism and dynamic response addressed the significance of unequal lateral impact load. The usual circular reinforced concrete members are used as the model to perform the drop-weight impact test. The specimens' crack pattern, failure mechanism, impact, deflection, and strain time–history curves are obtained. Findings show that between the impact point and the adjacent support, shear fractures occur that fail in shear mode. Shear cracks are based on impact velocity, longitudinal reinforcement ratio, and stirrup ratio. One type is more destructive to members and nodes. A shear fracture occurs when a longitudinal reinforcement fractures towards the closer support. The effects of impact velocity, longitudinal reinforcement ratio, and stirrup ratio on the dynamic impact response are studied. The experimental results may help improve structural member impact resistance. The critical section (right side) computed the static shear resistance using shear force, whereas the maximum external load resistance determines static bending moment resistance. Understanding how circular members fail to be subjected to unequal lateral impact loads provides insight into circular RC members' impact design and damage evaluation.

Keywords: impact duration, shear crack, impact test, failure mode, energy absorbed, locomotive train, static bending, shear strength

1 General

Concrete structures may be exposed to dynamic loads from vehicle impacts or impulsive loads from objects falling. These loads should be addressed while designing various structural components. Physicists say that impacts

have a short duration, high force levels, quick energy dissipation, and abrupt changes in body velocities (Bhatti et al., 2011). Many elements affect an impact event, including stress wave propagation, local elastic/plastic deformation, frictional energy dissipation, and other energy losses. Some reinforced concrete RC structures must be constructed to withstand impact loads caused by falling boulders in mountains or huge loads in factories, derailed trains, high-speed intercity trains, and intercity rail transit. The dynamic response of structural elements under ultimate stresses is unavoidable due to functional

Journal information: ISSN 1976-0485 / eISSN 2234-1315

*Correspondence: eng.khalil670@hotmail.com; yhliu@swjtu.edu.cn

¹ School of Civil Engineering, Southwest Jiaotong University, Chengdu, China
Full list of author information is available at the end of the article



© The Author(s) 2022. **Open Access** This article is licensed under a Creative Commons Attribution 4.0 International License, which permits use, sharing, adaptation, distribution and reproduction in any medium or format, as long as you give appropriate credit to the original author(s) and the source, provide a link to the Creative Commons licence, and indicate if changes were made. The images or other third party material in this article are included in the article's Creative Commons licence, unless indicated otherwise in a credit line to the material. If material is not included in the article's Creative Commons licence and your intended use is not permitted by statutory regulation or exceeds the permitted use, you will need to obtain permission directly from the copyright holder. To view a copy of this licence, visit <http://creativecommons.org/licenses/by/4.0/>.

needs. The latitudinal impact is a dynamic load that may cause major damage and the possible collapse of buildings and structures. Many experimental, analytical, and computational investigations have been done to understand better how RC members respond to impact loads (Anil et al., 2018; Bin & Zeng, 2014; Daudeville & Malécot, 2011; Dok et al., 2021; Isaac, 2014; Kishi & Mikami, 2012; Zhao et al., 2019). Currently, a considerable agreement exists on the response properties of RC beams under impact loads. Analytical methods to estimate impact force and examine concrete member behavior have been suggested before (Bischoff et al., 1990; Pham & Hao, 2016a). The dynamic behavior of structures under impact is often complicated and intimately connected to the structure's type and material properties. Also, many issues regarding RC's structural impact and dynamic material characteristics remain unresolved. Damage levels range from zero to moderate, severe, and catastrophic collapse with increasing maximum deflection. To adequately analyze the structural safety of RC members under impact loading, both flexural capacity and maximum deflection response must be estimated (Fujikake et al., 2009). Numerous researchers and scholars have explored RC structures under severe loads (e.g., earthquakes, blasts, impact) (AL-Bukhaiti et al., 2021; Dok et al., 2021; Heng et al., 2021; Jia et al., 2021; Liu et al., 2020, 2021; Tran et al., 2021; Wang et al., 2021; Yanhui et al., 2022; Zhao et al., 2021).

Researchers noted that all impact specimens developed inclined shear fractures at the impact point and eventually displayed shear plugs. Many types of research have concentrated on RC specimens with axial loads (Cai et al., 2018; Zhao et al., 2017; Zhu et al., 2021). Pham and Hao (2016a) studied the prediction of the impact force on reinforced concrete beams from a drop weight. A study aims to predict the maximum impact force on reinforced concrete beams subjected to drop-weight impact. A new empirical model including an extended and simplified version is proposed. The model was verified against a database collected from the literature, including 67 reinforced concrete beams. Maximizing stirrup distance and diameter reduces brittle failure under impact loads. Kinetic energy and static bending capacity are used to predict maximum mid-span deflection by Wongmatar et al., (2018). Wuchao Zhao et al. proposed a new approach for predicting the peak response of RC beams that have been exposed to impact loading. The technique can accurately predict the maximum mid-span deflection under impact loading, compared with 143 impact tests. Peak impact force is somewhat overstated in the prediction, which may be employed in the anti-impact design (Zhao et al., 2019b). Zhan et al. used an instrumented drop-weight impact machine to evaluate the high-speed

impact failure of reinforced concrete (RC) beams. Input impact energy and static flexural load-carrying capability were used to calculate maximum and residual beam deflection (Zhan et al., 2015). Other researchers' experimental results verified the equations' applicability. The lateral impact caused shear or punching shear failures in several of these studies. Contrasting flexural failure with ductile deformation, shear failure of concrete members is a brittle failure that frequently causes catastrophic destruction. With the rapid expansion of global infrastructure, an increasing number of RC structures are exposed to varied impact loads over their lifetime. Due to design flaws, these structural members seldom survive accidental loads. As a consequence, the behavior of reinforced concrete structures to lateral impact is of curiosity. The low-elevation vehicle causes flexural-shear failure. This situation is distinct from mid-span flexural failure. The lack of systematic study on shear failure and associated cracking processes of RC members under impact is apparent from the few experimental studies described in the literature. There has been a rise in the number of large-scale accidents involving reinforced concrete members between vehicles, ships, and trains, posing a greater danger to important transportation infrastructure. A lot of studies explain the dynamic response for impact force coming from ships or vehicle trucks collisions on reinforced concrete members (Chen et al., 2020; Roy et al., 2021; Sha et al., 2021; Xia et al., 2018).

To the present, no investigations have looked into the effect of unequal lateral impact force on RC members' impact response. Furthermore, most prior drop hammer testing of RC members was done on mid-span members, whose impact site varied greatly from prototype constructions. Nevertheless, no one has highlighted the consequences of train collisions on RC members prior to this research. The design of railway structures for train collision is more significant with the increase of the striker's mass and impact velocity to the structural member. The impact position plays an important role in the derailment behaviors of train vehicles. The derailment accident is more likely to happen when the striker collides laterally on the front of the leading module (Hou et al., 2020; Zhang et al., 2021). The originality of this research is that it included an experimental test of the effect of a train collision as an unequal lateral impact force on circular reinforced concrete members, as shown in Fig. 1. As a result, at Taiyuan University of Technology's Structural Laboratory, a well-instrumented drop hammer test program was designed to investigate the impact response characteristics and shear modes of unequal lateral impact force on circular RC members. This research conducted a drop-weight impact test on four circular RC members with dynamic flexural failure mode specimens to

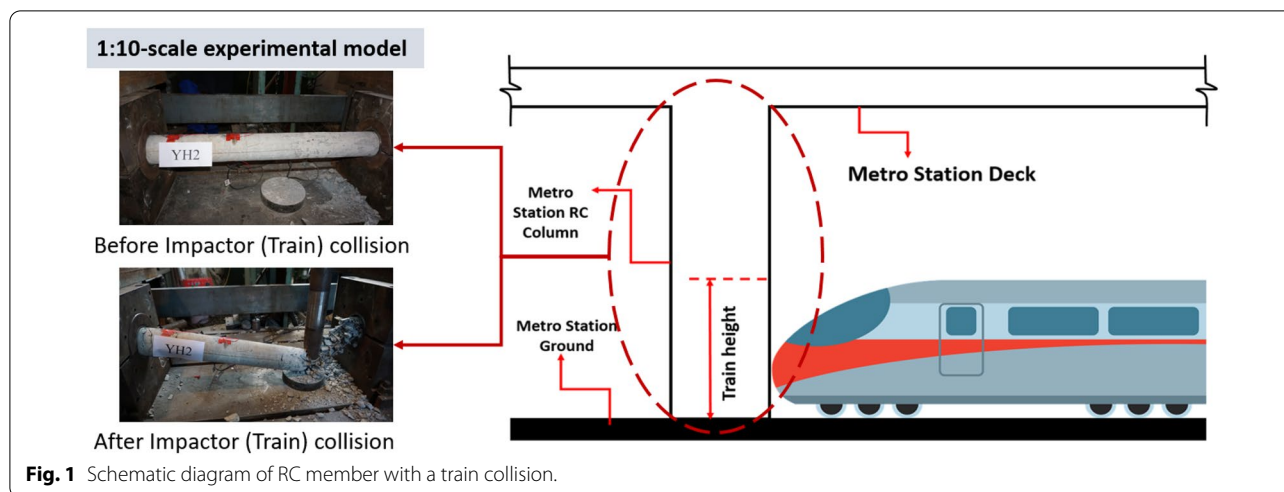


Fig. 1 Schematic diagram of RC member with a train collision.

investigate their behavior when exposed to unequal lateral impact loads. The impact velocities varied from 4.4 to 6.2 m/s, loads, deflections, and strains were evaluated throughout the testing. The impact response of RC members was studied as a function of drop height, longitudinal reinforcement, and stirrup ratio.

1.1 Research Significance

The shear-span ratio for the structural features of high-speed rail derailment impact is 1/5 to 1/4. When the high-speed rail derails, it is highly likely to occur at the turnout of the railway track, and bullet train crashes into the station building. The typical reinforced concrete station building column diameter is 1.2 m, and height is 10 to 12 m. The train's impact height is 1.8 m. The impact body is heavy, and the affected body is light. The train involved in the incident had three carriages. This means that the maximum collision velocity is 350 km/h. Given the features mentioned above and the test device's maximum span of 1500 mm, this work scales the reinforced concrete members and impact energy by 1:10 to investigate their dynamic response to high-speed impact loads. The main objectives of the proposed experimental study are to determine the failure mechanism and dynamic response of circular cross-section reinforced concrete specimen's characteristics under unequal lateral impact loads (2/9 clear span). The test tracks crack development, failure status, impact, and deflection time histories.

2 Materials and Methods

A total of four reinforced concrete specimens with circular cross-sections will be used in the impact test. The test specimens are denoted by the letters "YH", where "Y" stands for "circular" and "H" stands for "concrete". To maintain consistency, each test specimen is

poured with the same material. The test focuses on the impact resistance of specimens with unequal lateral impact force from varied impact heights, longitudinal reinforcement ratios, and stirrup ratios. In the test, the specimen has fixed support at both ends, a design length of 1500 mm, and support lengths of 200 mm at both ends. The clear span is 900 mm, and the impact point is placed at 2/9 of the clear span 200 mm from the right end support and 700 mm from the left to simulate a high-speed train locomotive (CHR2) collision (Kang et al., 2019).

The specimen's cross-sectional diameter is 114 mm, and each test specimen has 6 HRB235 steel bars evenly distributed along the specimen's ring direction, as illustrated in Fig. 2. The stirrup has a 4 mm diameter. A smooth steel bar is used instead of a hot-rolled ribbed steel bar since finding one with a diameter of 4 mm is difficult. The thickness of the concrete cover is 12 mm. Table 1 lists the dimensions and reinforcing details of the specimens. The reference specimen YH2 is utilized, and only one parameter differs from YH2 compared to the other specimens. The impact energy shown in Table 1 includes frictional energy loss, computed using energy conservation principles. Referring to the effect of the bonding strength influence, the term bond commonly refers to the adhesion between concrete and steel, which resist the slipping of steel bar from the concrete (Alharbi et al., 2021). This bond is responsible for transferring stresses from steel to concrete, thereby providing composite action of steel and concrete in RC members. The structural behavior of reinforced concrete elements requires the interaction between steel reinforcement and concrete. Impact forces in the area of separating cracks and bending cracks are carried by the reinforcement and transferred into concrete by bond action.

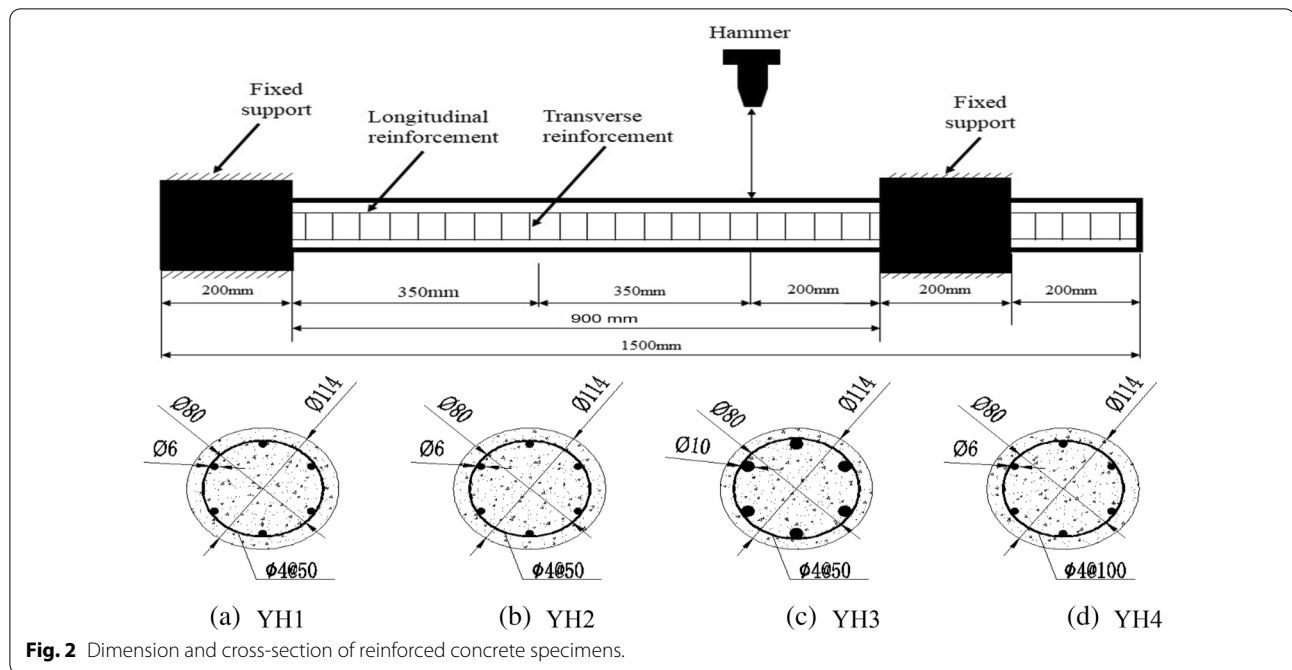


Fig. 2 Dimension and cross-section of reinforced concrete specimens.

Table 1 List of sample design.

No.	Longitudinal reinforcement ratio	Volume stirrup ratio	Impact High (m)	Impact velocity (m/s)	Impact energy (J)
YH1	1.67% (6Ø6)	1.26% (Ø4@50)	1.0	4.42	2646
YH2	1.67% (6Ø6)	1.26% (Ø4@50)	2.0	6.26	5292
YH3	4.61% (6Ø10)	1.26% (Ø4@50)	2.0	6.26	5292
YH4	1.67% (6Ø6)	0.63% (Ø4@100)	2.0	6.26	5292

Impact velocity in the table $v = \sqrt{2gh}$; impact energy $E_{impact} = mgh$; h is the impact height.

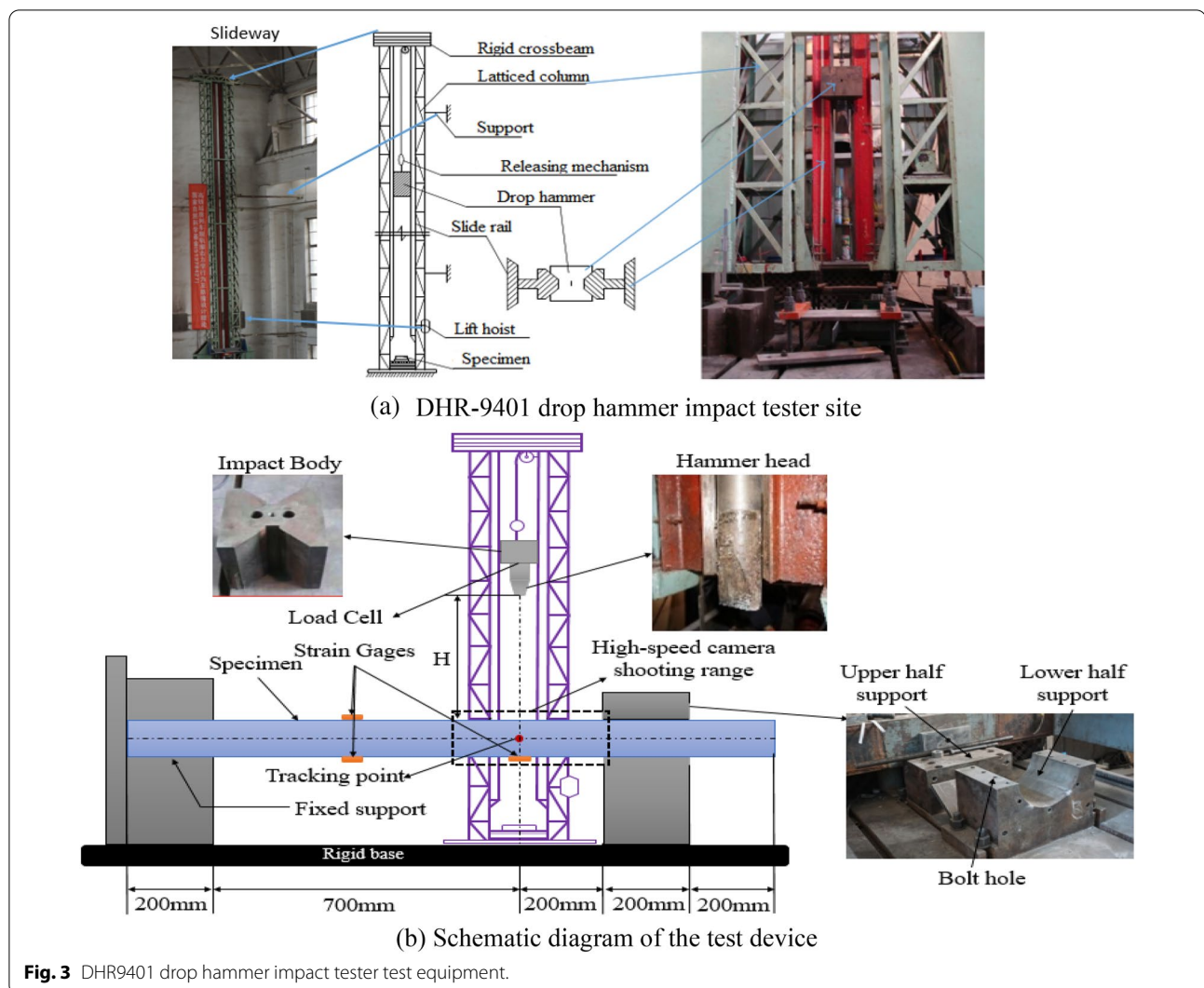
2.1 Impact Energy

Impact load was delivered to circular RC specimens at two distinct input impact energy levels by dropping a 270 kg steel hammer from two different heights of 1.0 and 2.0 m. While the input impact energies are being determined, two damage patterns, moderate–severe and severe, are expected to be observed. It has been predicted that moderate–severe shear cracks will form in circular RC specimens at lower input impact energies. It has also been suggested that when impact energies increase and longitudinal and transverse reinforcement changes, the severity of shear cracks in circular RC specimens would increase. Using two different impact energy, the dynamic response of circular RC specimens could be investigated for various failure mechanisms and damage patterns.

2.2 Test Device, Loading, and Measuring Scheme

This impact test was completed on the DHR9401 drop hammer impact-testing machine, as shown in Fig. 3.

The height of the DHR9401 drop hammer slideway is 13.47 m, the effective drop distance is 12.60 m, and the corresponding impact velocity can reach a maximum of 15.7 m/s, which can meet the requirements of low-speed impact-testing in a wide range. According to energy conservation, the impact height was chosen as 2.0 m; thus, the impact velocity was calculated as 6.26 m/s. The test frame is a portal frame composed of two vertical lattice steel columns and rigid beams. The frame is connected to the surrounding buildings through multiple supports and has good overall rigidity. The inner side of the rigid frame column is provided with a steel rail slide. The slide has a surface roughness of 0.8 after grinding. The drop hammer with a "V" groove adopts a sliding fit with the track. The error of the track along the entire height direction is only (2 mm). The body falls smoothly, the impact velocity of the drop hammer is very repeatable, and the error is within 2% compared with the calculation as shown in Fig. 3a. The drop weight is lifted by a small hoist driven by



a motor, and the release adopts an electromagnetic automatic control mechanism, which is easy to operate, safe and reliable. There is a large-volume concrete foundation at the bottom of the frame, and a yellow sand cushion is set between the rigid ground and the foundation. The vibration isolation performance is good, and the surrounding instruments will not be affected by the impact of the falling hammer. A 500-mm-thick steel platform is placed on the foundation as a test piece placement platform, and there are grooves on it to install different types of supports according to the needs of the test. The lower part of the support is fixed on the rigid platform, and a linear bearing is installed in the support. This bearing can restrain the displacement of the component in all directions except the axial direction to realize the boundary condition of fixed support.

As shown in Fig. 3b of the device, the mass of the striker weights can be adjusted arbitrarily within the

range of (2~270 kg) and matched with the corresponding height to meet the impact energy requirements. The impact body is composed of a drop hammer and an impact head. The drop hammer is made of (45# forged steel); the impact head comprises large-strength chromium 15 (64HRC). Conspicuously, the striker weights (impact body, load cell, and impact head) weighed 270 kg. The test's drop mass and height were chosen based on a locomotive's mass (64 t) and train speed (80 km/h) while passing stations. The test was 1:10 scale, the impact energy was estimated to be (15.8 kJ). The shape of the impact head is a rectangular parallelepiped face, and the size is 80 mm × 30 mm × 80 mm. The contact surface size is 30 mm × 80 mm. The total weight of the striker in this test is 270 kg. A load cells sensor is placed between the impact head and the drop hammer to measure the impact force. The test specimen support is made of (Q235) steel. The support is

divided into upper and lower parts (Fig. 3b), and there is a bolts connection between the upper and lower parts. The bolts provide pre-tightening force for the two parts of the support, effectively improving the friction between the support and the test specimen. To a certain extent, it can restrain the component from moving in the axial direction. Fig. 3a shows the assembly diagram of each component of the impact test site.

This test employs an electromagnetic winch to absorb and raise to a predetermined height at a consistent rate while letting go of the impact body. The specimen is then released. The free-falling impact body slams against the component. The test is primarily concerned with the following information:

- 1) A force sensor is attached between the impact head and the drop hammer to measure the impact force–time history curve, as illustrated in Fig. 3b. The force sensor acquires data at a million per second. The TDS420 dynamic data storage oscilloscope records and saves the amplitude-modulated signal from the strain amplifier.
- 2) Image recorded by a high-speed camera situated in front of the specimen’s impact point and shear

span, showing the full process from deformation to destruction. 2500 frames/s firing frequency.

- 3) The displacement time history curve of the impact body and test specimen is generated by processing the deformation image of the test specimen acquired by the high-speed camera every 0.4 ms. To capture specimen deformations, three-track white points at intervals of 150 mm were marked on the specimen, as shown in Fig. 3b.
- 4) A combination of Microsoft Excel spreadsheets, Origin 19 pro, CAD design applications, and image editing software was used to handle the data. The data were analyzed qualitatively and quantitatively.

2.3 Material Properties

2.3.1 Concrete

Concrete test blocks were made by numerous cubics (150 × 150 × 150 mm) at the same time with members’ casting as listed in Table 2; the concrete strength grade is C30. The test is measured according to the "Standard for Test Methods of Mechanical Properties of Concrete" (GB50081-2010); after 28 days of water curing, the compressive strength test was performed as shown in Fig. 4a, with the measured average compressive strength of concrete for 28 days $f'_c = 55$ MPa.

2.3.2 Steel Bar

The test is carried out in accordance with the "Metal Material Tensile Test Method" (GB/T228-2010) (GB/T, 2020), as shown in Fig. 4b. The measured mechanical parameters of the steel bars are shown in Table 3, where d_o is the diameter, E_s is the elastic modulus, f_y is the yield

Table 2 Compressive strength of concrete cube.

Test block 1	Test block 2	Test block 3	Test block 4	Test block 5
56.11 MPa	54.29 MPa	50.96 MPa	54.72 MPa	57.11 MPa
Test block 6	Test block 7	Test block 8	Test block 9	Average
52.24 MPa	57.51 MPa	53.59 MPa	58.21 MPa	54.97 MPa



(a) Cube uniaxial compression test



(b) Steel bar tensile test

Fig. 4 Concrete and steel bar material test.

Table 3 Rebar performance indicators.

d_0 (mm)	E_s (GPa)	f_y (MPa)	f_u (MPa)	δ
4	180	520	684	0.213
6	200	380	509	0.227
10	188	325	412	0.224

strength, f_u is the ultimate strength, and δ is the elongation rate of steel bars. Strain stress test curves are shown in Fig. 5.

2.4 Details of Test and Analysis

The specimens are installed in the impact test machine to elucidate the dynamic response characteristics of the structural specimen under the unequal lateral impact, as shown in Fig. 3. The concrete in the compression zone of the specimen was crushed. Bending fractures enlarge and approach the compression zone. The specimen exhibits bending failure prior to the occurrence mentioned above. The shear fracture in the test specimen has penetrated,

indicating shear failure; when the ultimate deflection of the specimen exceeds (1.1%) of the clear span, it is determined that the specimen has failed due to bending.

2.5 Crack Development

This section discusses each specimen’s crack development process in detail, starting with the impact body and test specimens and ending with the specimens’ damage. Figs. 6, 7, 8 and 9 show the development form of the crack for every specimen as recorded by a high-speed camera, as well as a description of where the crack develops. Fig. 6 shows the YH1 crack development under an impact velocity of 4.43 m/s and an impact of 270 kg. Two vertical fractures occur at the impact point (when the impact body contacts the test specimen) at 0.4 ms. At 0.8 ms, a 36° oblique crack (take the angle between the crack and the horizontal direction) emerged on the right side of the impact point, and a 37.5° oblique crack appeared in the middle of the proximal support extending to the top of the specimen. It did not penetrate the vertical crack that happened

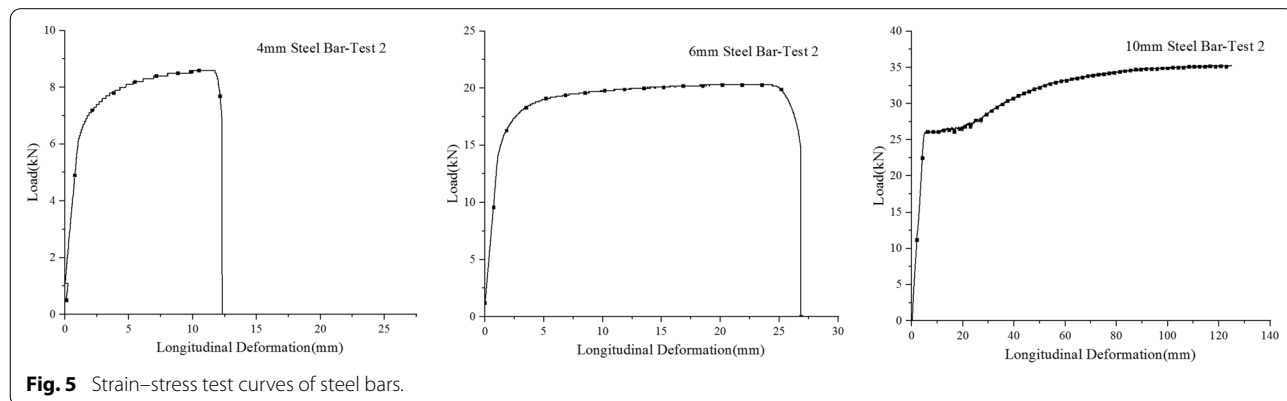


Fig. 5 Strain–stress test curves of steel bars.

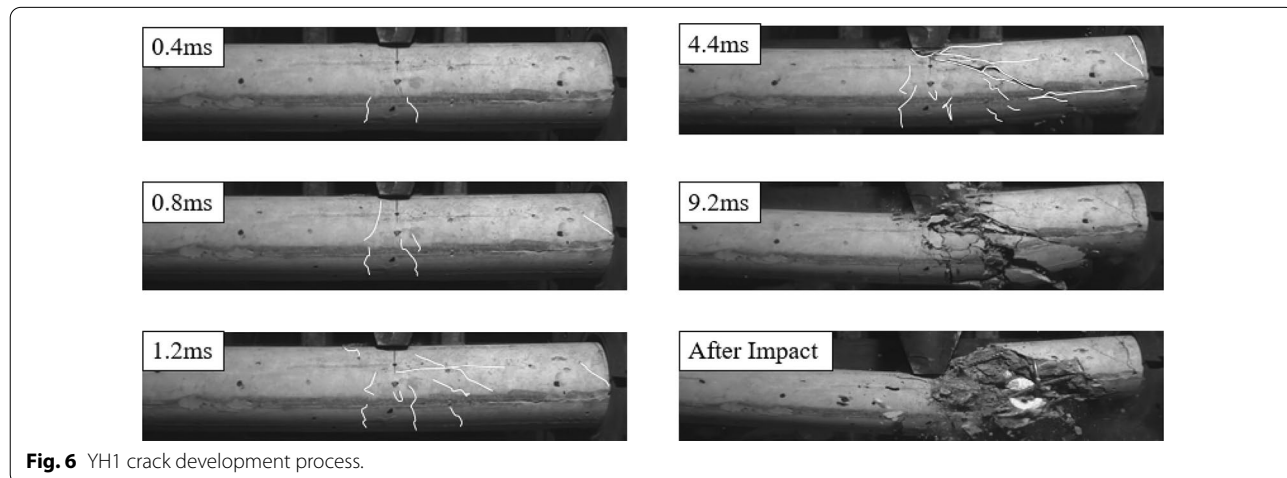


Fig. 6 YH1 crack development process.

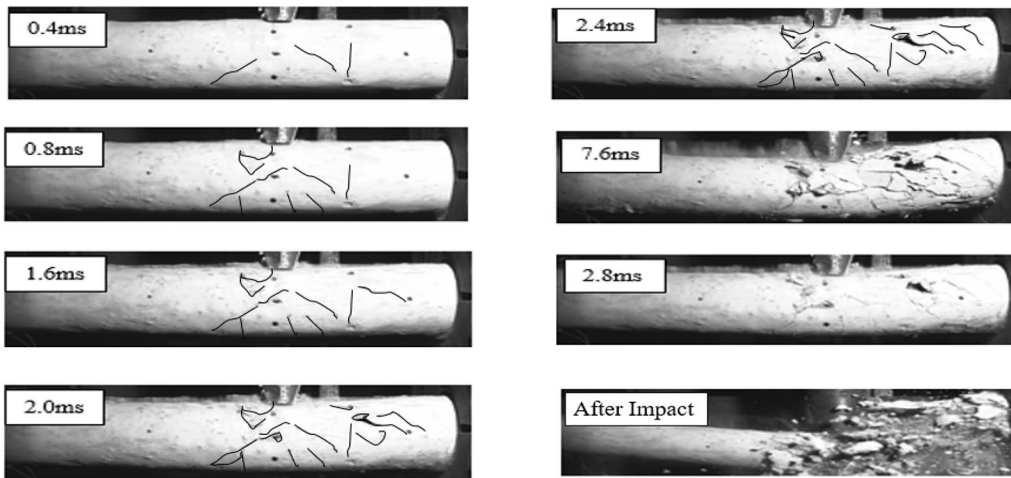


Fig. 7 YH2 crack development process.

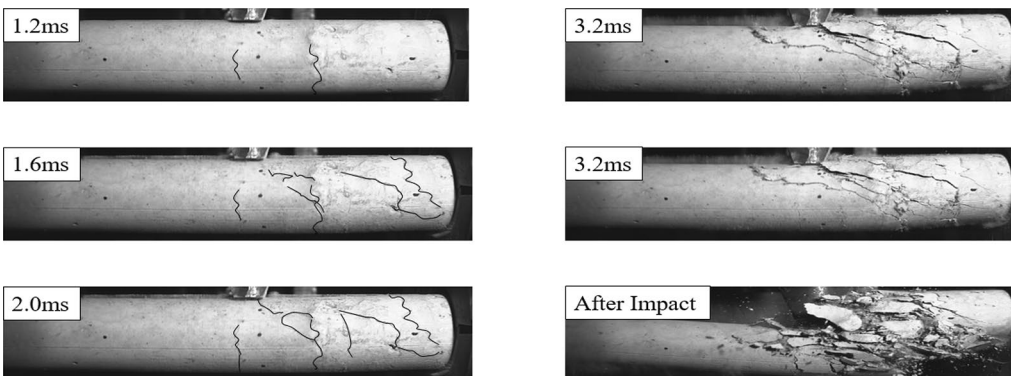


Fig. 8 YH3 crack development process.

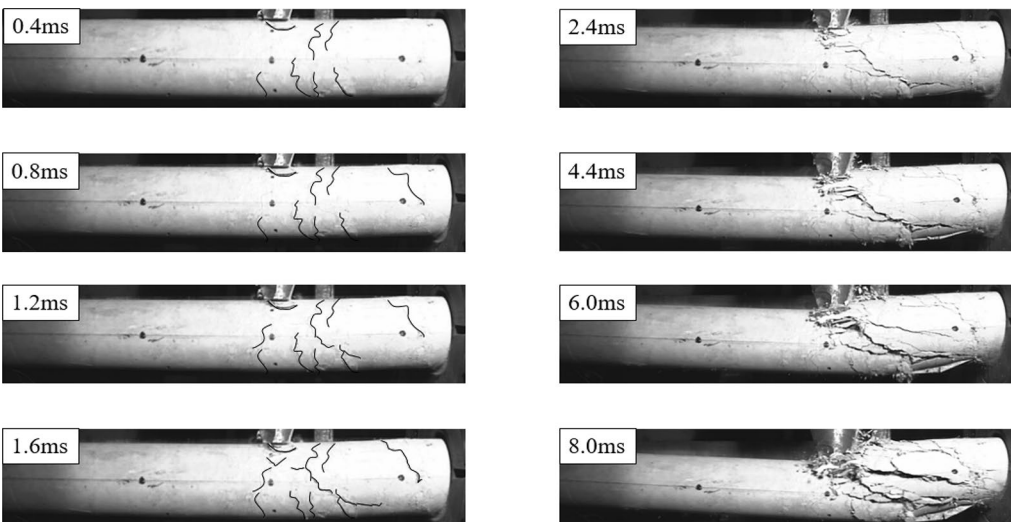


Fig. 9 YH4 crack development process.

at 0.4 ms, and it appeared on the bottom right of the impact point. After a short vertical extension, the tendency is to expand toward the impact point.

A 36.5° main diagonal crack appeared in the shear span to the right of the impact point, and new vertical cracks started to emerge near the specimen's bottom. The concrete at the impact location was still undamaged. This resulted in a 36.5° failure surface on the right side of the impact point, indicating that the specimen was fractured. By 9.2 ms, a web of vertical and oblique cracks had developed between the impact point and the failure surface, concrete fragments had splattered, and steel bars had been revealed. After the impact, the concrete shattered into a powder, the steel bars bent but did not break, holding the fractured concrete together, and the stirrups remained intact. Overall, the specimen is severely damaged, but only between the impact point and the damaged surface.

Fig. 7 shows the YH2 crack development under impact velocity 6.26 m/s and impact mass 270 kg. At (0.4 ms) after the impact head contacts the specimen, two symmetrical diagonal cracks emerge at the impact point. Vertical cracks extend from the top and bottom of the specimen on the left side of the impact point to the middle of the specimen. Near the impact point, many vertical cracks emerged at (0.8 ms). The concrete was substantially maintained at this time. Aside from the impact point, three parallel 51° diagonal cracks occurred on the support at 1.6 ms. The oblique cracks in the shear span initially extended at 51° from the specimen middle to the top and bottom. Two diagonal cracks are distributed on its right side; one starts from the middle of the specimen and faces the support, the bottom extends, and the other extends to the top of the specimen at the center axis of the right end support. The concrete cover between the impact body and the specimen has peeled off. At 2.0 ms, a 51° diagonal shear crack appeared. The crack extended up to the impact point and down to the right end support in 0.4 ms. The initial crack altered as it approached the top and bottom of the specimen. At 2.4 ms, the extension direction develops horizontally, forming a surface thoroughly. At 2.8 ms, new vertical cracks emerged at the region's bottom between the impact point and the right end support. In addition, the two diagonal cracks in contact with the support extended to inside the support. At this stage, intertwined cracks split concrete into desired shapes, and many through cracks cause concrete near the support to be divided into blocks. Some of the smaller concrete blocks collapsed. Until 7.6 ms, the concrete splattered, and the right support's steel bars were visible. Since the concrete failed, the impact energy was transferred to the steel bars, which started to pull the inner part of the right support to the left. So, after the collision,

the specimen's concrete is severely damaged and crushed, and the support's fixed part is pushed out for a distance.

Fig. 8 shows the crack development of YH3 at 6.26 m/s and 270 kg. At 0.4 ms, a vertical crack emerges just below the impact point, reaching the cross-3/5 section's height. A 56° oblique crack developed on the right side of the impact point, towards the impact point and the specimen's bottom. It was discovered at 0.8 ms that a 35° diagonal crack had developed in the shear span, between the impact point and the bottom of the right end support. There were two oblique cracks from the bottom of the right end support to the impact point at 27.5° and 56.5°, and a vertical fracture on the top right end support. At 1.2 ms, a 38° oblique major crack developed from the center to the impact point to the bottom of the specimen. However, the primary oblique crack penetrates at 1.6 ms.

On the support's bottom, the 27.5° oblique crack enters the 35° oblique crack next to it, and the top end continues to expand toward the impact point. The vertical cracks developed are neither extending nor widening. At 2.0 ms, as the shear span was increased, additional minor diagonal fractures emerged near the bearing on the right. Three through surfaces develop in 3.2 ms. At 3.6 ms, when the concrete between the through cracks splits into blocks, it loses strength. The steel bars bear the weight of the specimen and the impact body, causing the longitudinal bars to pull and drag the right end support to the left. The concrete from the right side to the failure surface collapsed, but the steel bars held firm. The specimen is severely damaged between the impact point and the damaged surface.

Fig. 9 depicts YH4 crack growth at 6.26 m/s and 270 kg. At 0.4 ms, the concrete cover layer is crushed at the impact point; many vertical cracks develop between the supports on the right side of the impact point. An up-and-down 60° major oblique crack appeared at 0.8 ms, at the shear span right of the impact point. The specimen's top and the central axis were both reached by a 56° oblique crack. In the 1.2 ms period, the right side vertical cracks on the impact point gradually merged, and the remaining vertical cracks on the impact point continued to extend to the impact point; the 60° main oblique crack's upper and lower ends changed development trends, with the lower end first extending in the direction of a 36° angle, and then both upper and lower ends developing horizontally, continuing to rise.

At 1.6 ms, the top end of the main oblique crack enters the compression crack, and the main diagonal crack penetrates. After 2.4 ms, the failure surface expanded, and the specimen's bottom concrete was split longitudinally. For the right side of the impact point, only steel bars supported the concrete. After 2.4 ms, the failure surface continued to widen, and the concrete at the bottom of the specimen was

turn in the axial direction. The concrete had lost its bearing capacity for the right side of the impact point and was only borne by steel bars. A 26.5° oblique fracture occurred between the impact point and the right end support at 4.4 ms. At 6.0 ms, all oblique cracks are penetrated, and their lower ends reach the right end support and extend within. The concrete between the impact point and the right end support was shattered at 8.0 ms. The steel bar pushes the right end support out a distance, crushing the concrete between the impact point and the support and seriously cracking the pushed-out concrete in the support.

To sum, all specimens fail under shear, with the failure surface extending upwards from the impact point. Once YH1 fails, the failure surface is located at the bottom of the near support. YH2’s failure surface collapses near the support’s bottom, and the crack develops into it. Thus, following the impact, the concrete is crushed, and the fixed section of the support is pulled out. The lower failure surface of YH3 is closer to the support than YH1. The right side concrete shattered, but the steel bars stuck firmly. The YH4 crack ruptured the specimen’s bottom concrete longitudinally. A cracked concrete was lying between the impact location and support on its right side. That distance between the impact point and the support is crushed, and that pushed-out concrete in the support is severely cracked. The YH2 and YH4 failure surfaces dissipate around the support’s bottom, and the fracture extends through the support. Decrease specimen damage by increasing impact height and reinforcement ratio. Increasing the stirrup ratio does not affect the initial impact but may minimize concrete crushing. The shear cracking inclination is proportional to the specimen stiffness and impact velocity. Shear cracks may occur in three different ways in slender beams with a significant shear-span ratio (Yi et al., 2016). There are two kinds of shear fractures in this paper: (1) diagonal shear plug cracks at the loading point (type I); (2) inclined shear span fractures in contact with the specimen (Type II); Fig. 10 shows shear cracks that extend along the top and bottom of the longitudinal steel bars of the impact point and the direction of the adjacent support (Type II).

The angles of the main oblique cracks of the four specimens are 36.5°, 51°, 38°, and 60°, respectively. The angle variations are impacted by the specimen characteristics as follows: when the impact velocity increases and other variables stay constant, the angle of the major oblique crack increases; when the longitudinal reinforcement, stirrup

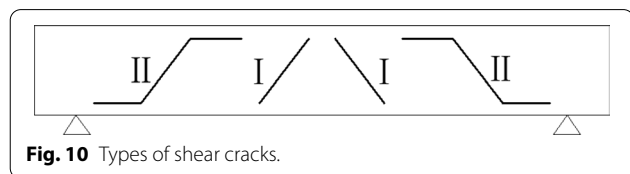


Fig. 10 Types of shear cracks.

ratio increases, and other conditions remain constant, and the angle of the main oblique crack decreases. In summary, reducing impact height and increasing the reinforcement ratio may reduce specimen damage. Increasing the stirrup ratio does not show a significant effect at the initial stage of the impact on the specimen; to a certain extent, it can reduce the degree of concrete crushing. It can be inferred from the experiment that the angle of the shear crack is related to the stiffness of the specimen and the impact velocity the specimen bears.

2.6 Failure Modes

2.6.1 Control Specimen YH2 Compared

Fig. 11 shows comparison of failure mode for the specimens YH1, YH3, and YH4 with the control specimen YH2 as follows:

- YH1 with control specimen YH2

Aside from the impact height, YH1’s impact height is half that of YH2, and all other variables are the same. It has less vertical cracks, and its width is smaller than YH2, and the bottom of the left end of YH2 has been compressed, and the steel protective layer is partly peeled off. YH1 lacks this effect; just the impact point is visible. YH2 deflects more than YH1 in the left portion. Both specimens’ failure surfaces are produced to the right of the impact point. YH1’s failure surface extends to the impact point and shear span. Unlike YH1, YH2’s failure surface has been extended into the proximal support. Therefore, the right part of the damaged surface of YH1 stays reasonably undamaged, but the concrete of YH2 crashes from the impact point to the right end of the support area. The right end support’s inner fixed part is damaged. Two rings of stirrups are visible on YH1, and all stirrups from the YH2 impact point to the support are exposed. That seems to be, the impact height increases, as does the damage range. So, as impact height increases, the primary oblique crack bottom moves to the right. Having more vertical cracks causes greater damage locally and a wider impact range.

- YH3 with control specimen YH2

The reinforcement ratio of YH3 is 2.76 times that of YH2, and all other criteria are the same. Vertical crack YH2 extends to the center axis of the left end support, whereas the length of YH3 vertical crack is 1/3 of member height. The vertical crack stops growing downwards when it reaches 30 mm in length. YH2 has a higher deflection than YH3 in the left part of the impact point. Both specimens’ failure surfaces are to the right of the impact point. After the YH3

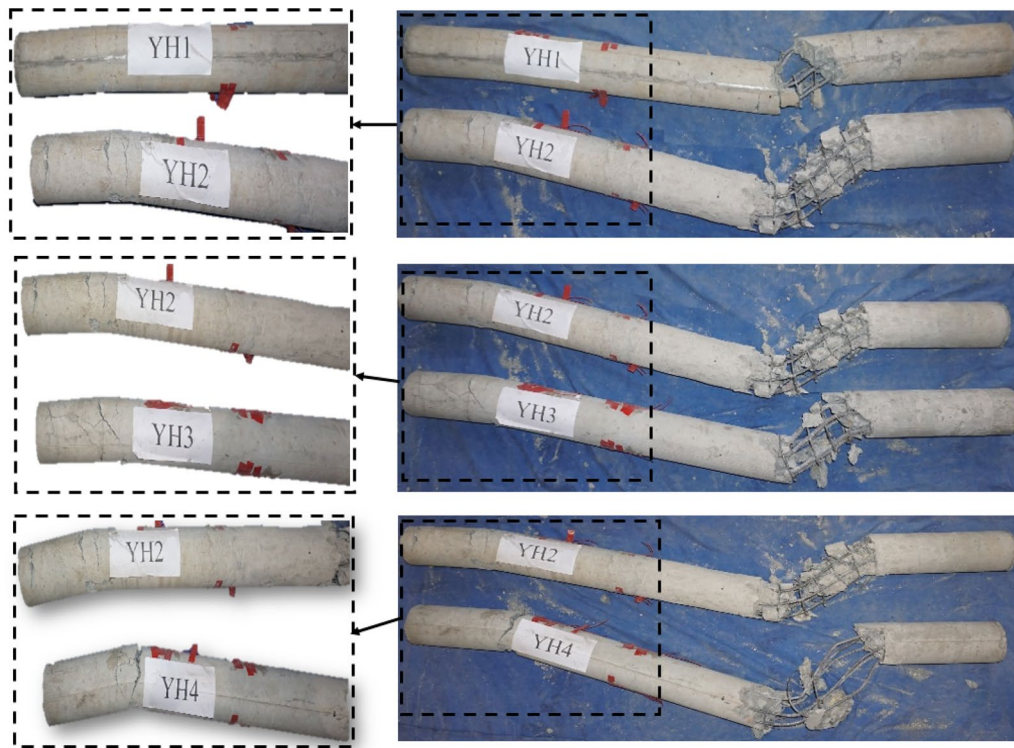


Fig. 11 Compares the failure modes of YH1, YH3, and YH4 with the control specimen YH2.

had been impacted, the cross-sections were complete, with upper and lower ends in the shear span. YH3's tensile length of longitudinal reinforcement is shorter than YH2's, and only three stirrup loops are visible. It illustrates that when the longitudinal reinforcement ratio increases, the local range damage decreases.

– YH4 with control specimen YH2

YH4 has half the hooping rate of YH2, and the other criteria are the same. This crack is wider and continues straight to the bottom longitudinal bar at the left end of the support. As a result of the compression, a part of the concrete is crushed, developing a vertical failure surface, and the specimen completely loses its supporting weight. Ability to immediately contact the barren ground after impact. Due to the decrease of stirrups, the section between the impact point and the damaged surface cannot bear greater force, and the undissipated energy is further supported to the right end via the steel bars. In YH4, the crack extension is wider than YH2 and reaches into the interior of the right end support due to the stirrup transmission. The stirrups in the concrete collapse area have collapsed. Increasing the hoop ratio increases the specimen's impact resistance.

The failure surface of YH1 and YH3 is at the impact point, and the lower end is inside the shear span. The higher end of the damaged surface of YH2 and YH4 is at the impact point, and the lower end immediately approaches the bottom of the near support. The oblique crack continues through the support, and in addition to the major oblique cracks, there are several vertical cracks.

2.6.2 Final Failure Modes of Specimens

Fig. 12 shows the overall damage of specimens after impact load. It seems that all RC specimens have undergone devastating shear failure. The specimen is crashed to eliminate the concrete fragments' form. On the end of the specimen near the support, obvious shear oblique cracks penetrated and developed an oblique crack failure surface. Although vertical cracks appeared at the impact point's bottom and the support's left and right end, the impact point's bottom vertical crack did not expand. Due to the concrete failure between the impact point and the failure surface, the steel bar is stretched, and the specimen becomes a cantilever beam with force at both ends. A vertical crack appears on the support. The specimen's damaged areas are the left top of end support, the impact point to the failure surface, and the right top end support.

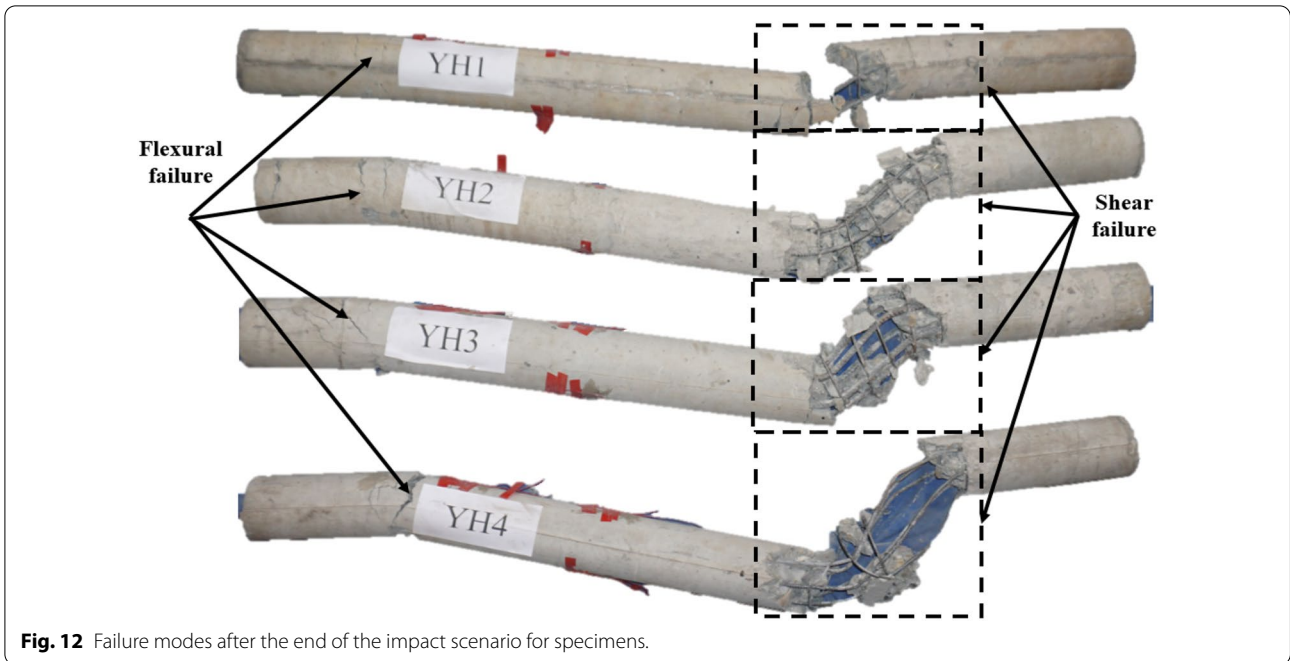


Fig. 12 Failure modes after the end of the impact scenario for specimens.

Also, previous experimental studies have reached the same result as the current study (Kishi et al., 2002; Liu et al., 2017; Yao et al., 2016).

3 Test Results and Discussion

3.1 Time History of Impact Load and Interaction Analysis

Impact force–time history curve is shown in Fig. 13 and can be roughly separated into three stages, as shown in the chart: (1) oscillation stage: at zero time, the impact body is in contact with the specimen, and the impact force rapidly achieves its highest value and then rapidly decays, resulting in a triangular pulse. (2) Stable stage: after the first peak value, the impact force varies within a particular range and lasts for a long time; this is the stage when most work is done. (3) Attenuation stage: after a steady stage, the impact force starts to attenuate and eventually drops to zero. Table 4 records the impact force’s specific peak value, the impact force plateau value (the average value of the impact force once it enters the stable phase), and time duration for specimens. It is the number of independent coordinates necessary to describe the masses’ displacement relative to their origin. SDOF systems have just one degree of freedom (degree of rigidity) in comparison to the affected members. The hammer’s equation of motion is:

$$m_h \ddot{u}_h + f(t) = 0 \tag{1}$$

where m_h , and \ddot{u}_h are \ddot{f} the hammer’s mass and acceleration. $f(t)$ is the recorded impact force by the hammer’s

load-cell. Whenever the hammer is dropped freely from a certain height, the speed varies as follows:

$$\dot{u}_h(t) = v_0 - \int_0^t \frac{f(t)}{m_h} dt. \tag{2}$$

In Eq. (2), v_0 is the hammer’s initial impact velocity. All specimens reach their maximal impact force in less than a second (5 ms). Although YH2 has double impact height, the peak impact force is 46kN higher than YH1. However, the impact force plateau was reduced by 5.37 kN, increasing the length (7 ms). Peak impact force increased by 14.47 kN, and plateau value increased by 5.98kN with increasing reinforcement ratio, but duration remained the same; YH2 was only 2 ms longer than YH3. Increasing the stirrups ratio reduces the impact force of YH2 by 50.13 kN, which is why the local stiffness of YH4 is greater than YH2. The specimen can bear more impact during hits. YH4’s platform value is 17.98 kN less than YH2, yet it lasts 5 ms longer. With the exception of YH2 and YH4, the impact force of YH1 and YH3 changes significantly in the platform stage and then rebounds strongly. The impact point and failure surface of the concrete collapsed parts of YH1 and YH3. However, the longitudinal bars of YH2 and YH4 has been revealed and increased. It seems that YH1 and YH3 steel bars are now yielding. For YH2 and YH4, when the failure surface is formed, the reinforcement provides the main resistance and enters the strengthening stage.

In other words, decreased plateau value and duration may be achieved by increasing impact height. Increasing the longitudinal reinforcement ratio increases the

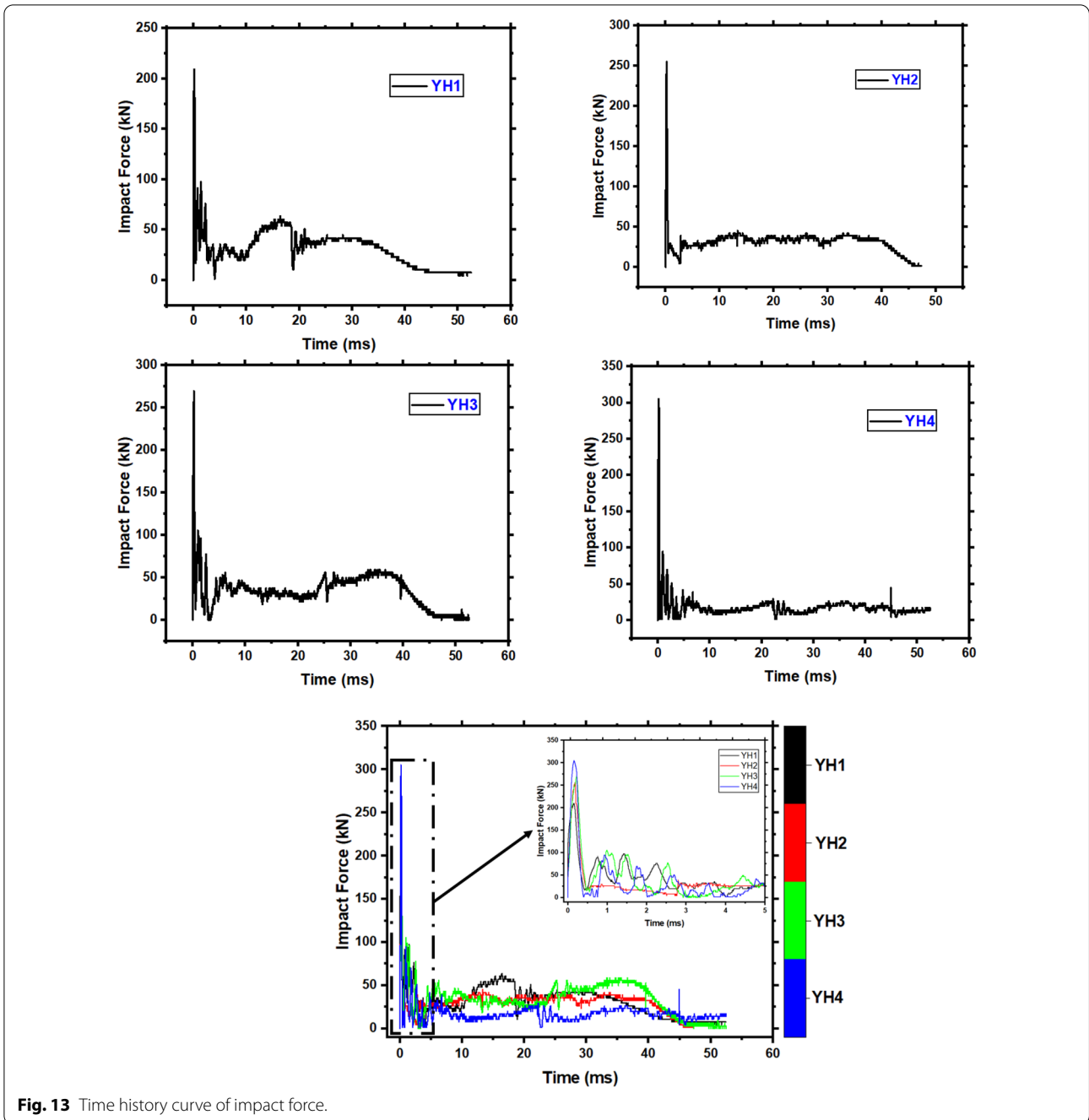


Fig. 13 Time history curve of impact force.

Table 4 Impact force data of specimens.

Specimen	YH1	YH2	YH3	YH4
$F_{max}(kN)$	209.30	255.30	269.77	305.43
$F_p(kN)$	39.55	34.18	40.16	16.20
$t_d(ms)$	30	37	35	42

peak impact force, also can improve platform value similar to previous impact test trends (Do et al., 2019; Roy et al., 2021; Zhao et al., 2019b; Zhu et al., 2021).

Increasing the stirrup ratio decreased the peak impact force, but the platform value has doubled due to the doubled stirrup ratio. The stirrup ratio has a bigger

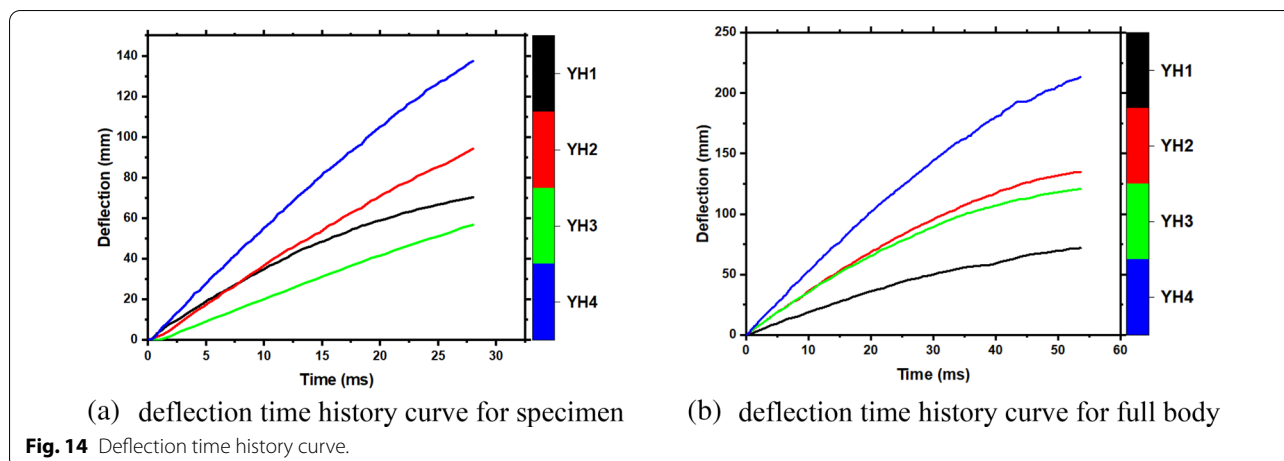


Table 5 Maximum deflection data of specimens.

Specimen	YH1	YH2	YH3	YH4
Maximum deflection of specimen (mm)	70.39	94.30	56.77	137.55
Maximum deflection of impact body (mm)	71.84	134.81	120.46	213.48

impact on the overall stiffness of the specimen than the reinforcement ratio (Wang et al., 2020).

3.2 Time History of Deflection Analysis

Fig. 14 illustrates the deflection time history curve with two graphs: (a) deflection time history curve specimens and (b) the impact body deflection time history curve. 92 mm below the impact point is the collecting point. The deflection is then calculated by tracking the specimen’s middle three points with the high-speed camera (see Sect. 2.2, Fig. 3b).

Table 5 lists the maximum deflection of each specimen and impact body. After the specimen is struck, the data will be lost in the later stage due to the concrete fragments collapsing.

In Fig. 14a, the data are just before the collected data points disappear. The impact body’s displacement data collecting begins from its contacts with the specimen and finishes when it stops falling. Fig. 14a shows that the deflection of all specimens increases before failure. Since YH3 data can no longer be acquired at 12 ms, the first 12 ms of the four specimens are evaluated.

The initial 12 ms deflections of YH2, YH3, and YH4 are linear, and the velocity is (5.02, 4.89, 5.45 m/s), respectively. The rate of change of YH1 tends to slow down gradually even though YH1 has broken, and it retains some bearing capacity.

The deflections of the four specimens are 43.69 mm, 63.92 mm, 56.77 mm, and 65.97 mm, respectively, at 12 ms. A failure surface has formed on all specimens. Deflection is not affected by the stirrup ratio in the early impact stage. Notwithstanding, the impact height, followed by the reinforcement ratio, greatly influences deflections. Fig. 14b collects data from the time the impact body contacts the specimen until it stops moving. Comparatively, the YH4 impact body deflects more than other specimens. Due to the YH4 stirrups ratio reduction, the concrete was completely damaged between the impact point and the right end support. In this configuration, the left side of the impact point behaves as a cantilever beam and bears some of the impact force. Thus, the YH4 far bearing’s negative bending fracture is practically penetrated and recorded the maximum deflection value compared to other specimens. At the same time, due to the impact body penetrating the specimen, the deflection value of the impactor also recorded the maximum value. In this way, impact height affects both initial and end deflection rates. Reducing later deflection and slowing deflection change may be achieved by increasing the reinforcement ratio. Increasing the stirrup ratio slows the maximum deflection. The reinforcement ratio has more effect on the specimen’s deflection. As stated before, the reinforcement ratio enhances lateral stiffness, which was apparent during the loading stage. That means the member was severely damaged and perfectly deformed due to the decrease in stirrups ratio (Huo et al., 2018; Liu & Xia, 2017; Pham et al. 2016).

3.3 Impact Force–Deflection Curve

To produce the impact–deflection curves, the impact force and deflection time histories were combined. The area under the curve represents the total energy consumed by the member during impact. Load–deflection

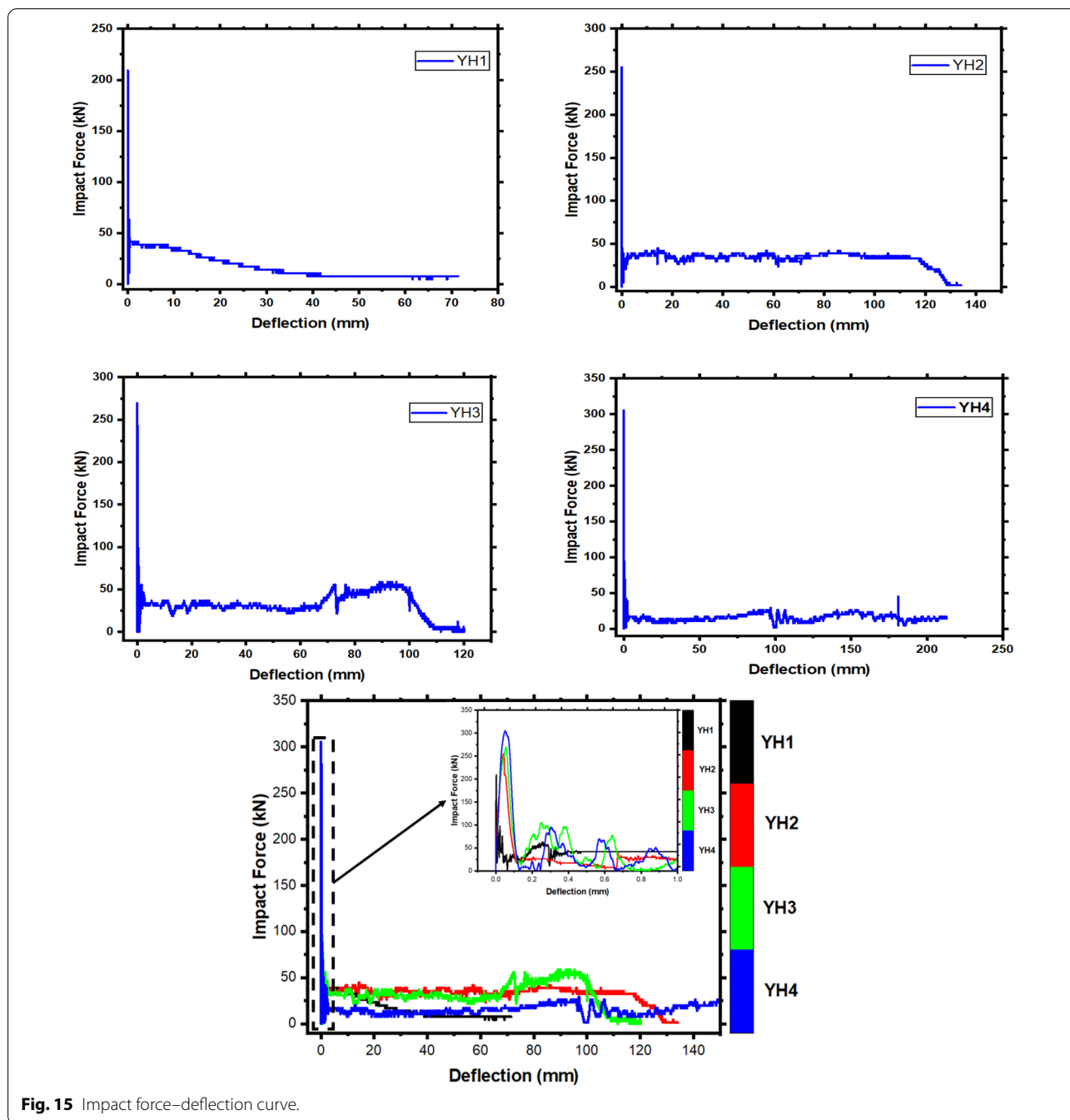


Fig. 15 Impact force–deflection curve.

curves can be used to calculate impact energy absorption. Curves may be classified as closed or open; Icten et al., (2009) presented a closed curve with an ascending loading section, a descending loading and unloading section. In this test, the deflection was gathered using a high-speed camera image after handling. Notably, the deflection and impact time history points did not coincide. So the deflection did not match the impact force–time history. As a result of this, the impact–deflection curve

is synthesized using Origin 19 pro’s interpolate module. The deflection and impact force curves are simultaneously based on ASCE/SEI 41Concrete Provisions (Yao et al., 2016). Fig. 15 illustrates the impact force–deflection curves of the specimens. It can be obtained that most of the energy absorbed by the specimen is transferred to the right end support. The energy absorption capacity of the specimen YH3 increases for the increase in the longitudinal reinforcement ratio. The specimen’s energy

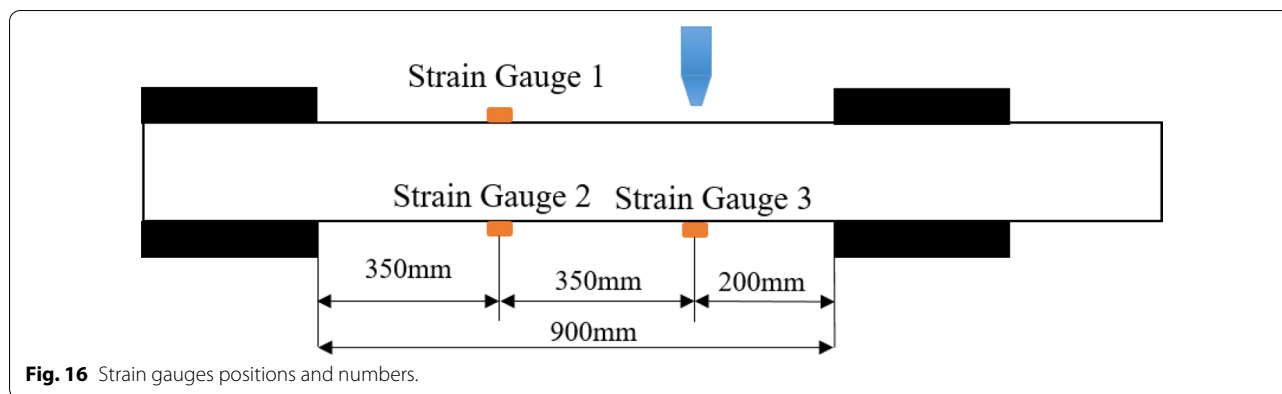


Fig. 16 Strain gauges positions and numbers.

absorption is subtracted from the reinforcement and stirrups' energy consumption. In both cases, the difference decreases as the reinforcement ratio decreases and grows as the reinforcement ratio increases. This occurrence demonstrates the argument as mentioned above.

Fig. 15 demonstrates that when the impact force peaks, all members deflect quickly, transferring 15–30% of the total kinetic energy from the impactor to the RC specimens. After the impact force, the member enters the plateau stage, and the remaining energy is transmitted when substantial deformation occurs. As seen above, increasing the longitudinal reinforcement ratio of the specimen increases its overall stiffness and hence its deformation resistance.

3.4 Time History of Strain Analysis

There were three strain gauges on the specimens with different positions to get different recording data to increase the accuracy of the experimental test results, as shown in Fig. 16. All strain gauges showed a bilinear pattern with a transition zone (AL-Bukhaiti et al., 2021). Both concrete and steel are sensitive to the strain rate effect under an impact force (Zhan et al., 2015). The specimens' strain curves were separated into three zones. The peak value (0.0021) for the YH1 specimen at strain gauge 1 was clearly at the moment of hammer contact with the specimen and then quickly decreased to the lowest value (-0.0017). Even yet, it's evident that after reaching the peak value, the curve for strain gauge 2 continues at the same value and duration. It indicates how much the specimen's ability has decreased after failure, and no resistance has been detected after flexural strain, as shown in Fig. 17. The maximum strain value was the same as the peak impact force point using the third gauge under the specimen at the impact point from the bottom (0.00255). After that, the strain time history curve decreased dramatically before rising again, and after reaching its maximum

value, it slightly recovered. It hesitated for a moment before returning to its maximum value. Then, with time, it steadily reduced until it reached a value of (0.0015).

Since YH2 has a higher drop hammer than YH1, it is evident that this specimen has the maximum strain curve as measured by gauges 3 and 1. Due to the specimen fracture, strain gauge 2 records a minimum value, and no resistance seems to be recorded on strain gauge 2's position. The capacity of the YH3 specimen to record decrease and increase values between (0.00067 and 0.0005) over the period (7 ms to 55 ms) is explained by the high longitudinal reinforcement ratio at the impact point gauge strain value.

Increasing longitudinal reinforcement influences strain capacity in preventing punched shear fractures in concrete members (Liu et al., 2021; Mylrea, 1939; Saatci & Vecchio, 2009; Xu & Zeng, 2014). Strictly speaking, with the emergence of punched shear fractures in concrete elements, the significance of longitudinal reinforcement becomes crucial in sustaining the specimen's stability (Do et al., 2019). For gauge 1 specimen YH3, the curve remains constant; for gauge 2, the strain value decreased after the time (5 ms) and varied between the values (0.00025 and -0.00024) throughout the period.

Compared to other specimens, the stirrup reinforced ratio effect on the peak strain value for YH4 specimens is reduced and does not exceed (0.0004) for all gauges. It is clear the gauges curves are drawn in the same way as with YH3, but the strain values are lower due to stirrups ratio decreases. Comparatively speaking, the contribution of the stirrups reinforcement ratio to the total strain capacity of the specimen is minor (2.5–5%) (Do et al., 2019).

4 Impact Duration

A striker's entire period of contact (impact duration) is measured from first contact until separation. Fig. 18 reveals that the impact lasted much longer than the specimen's main natural period. The overall mass of

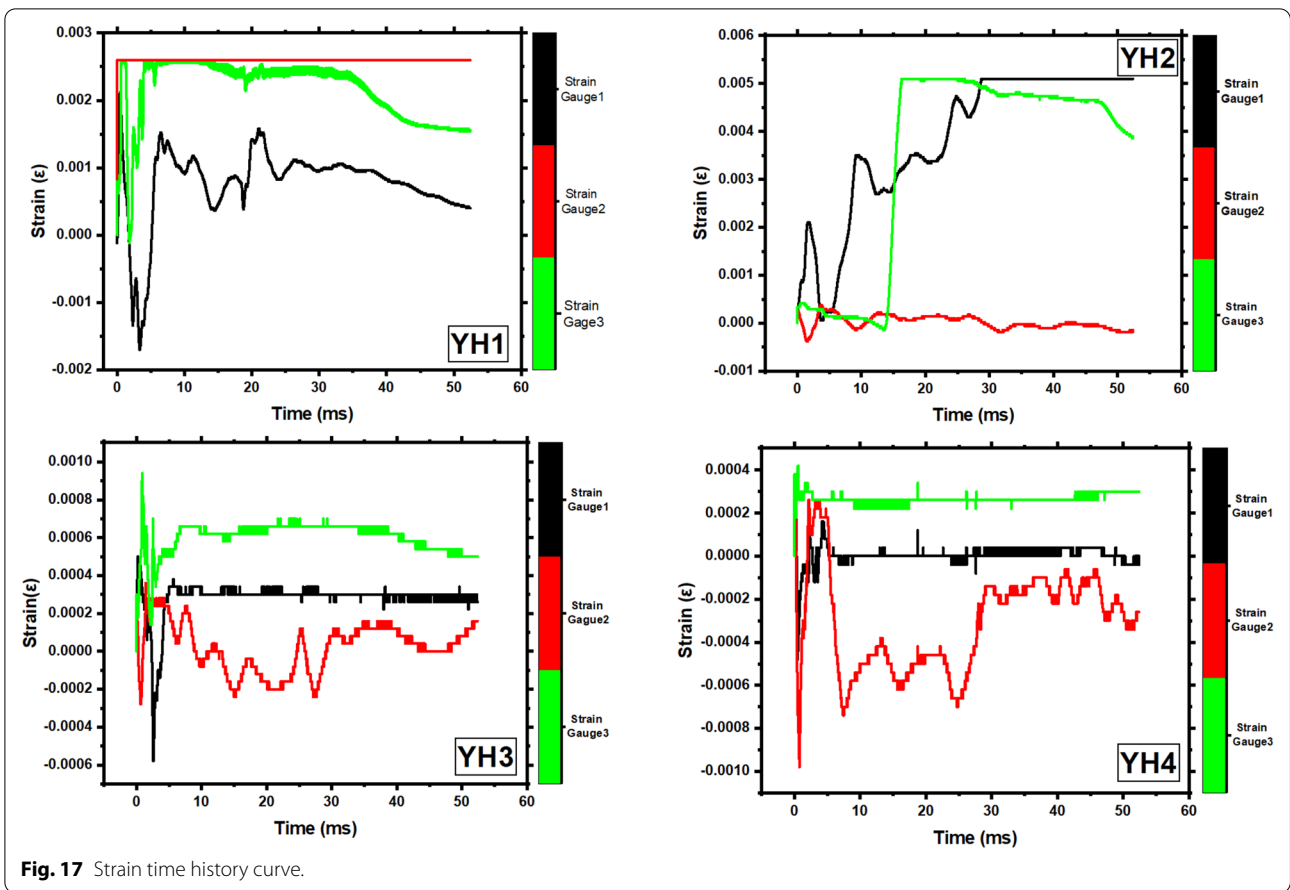


Fig. 17 Strain time history curve.

the specimen, including the striker mass, determines the total impact duration. During impact, the specimen deforms plastically. Plastic deformation extends the impact time. In a situation when the structure is subjected to a lateral force, the duration of the impact is determined exclusively by the damaged area (Zeinoddini et al., 2002).

Assume the train’s mass and velocity are considered. In this situation, the train’s mass (i.e., impact body, hammerhead) will contribute to a more extended impact period. Compare the slight oscillation displayed in Fig. 18, which reflects just the specimen’s dynamic behavior, with the entire duration of the impact, which shows both the specimen’s and the striker’s attributes. Fig. 18 shows the total duration is many times longer than the period of the minor oscillations. A structure subjected to an impact load without regard for the train’s mass would respond with dynamic properties different from those involved in a real impact occurrence. Aside from the failure situation, increasing unequal impact loading extends impact duration Fig. 18. More plastic deformation occurs with larger impact loads

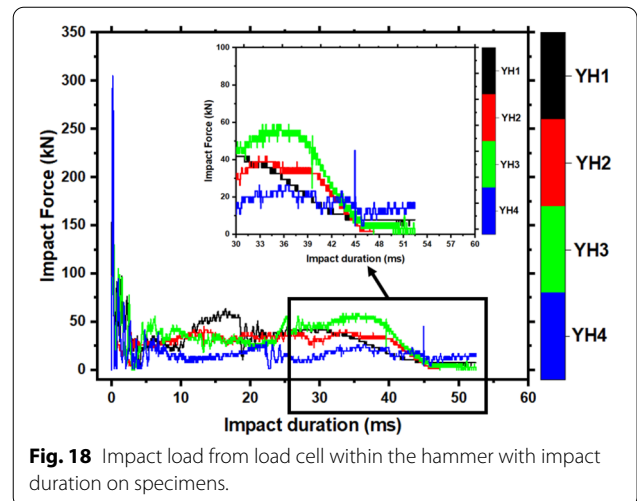
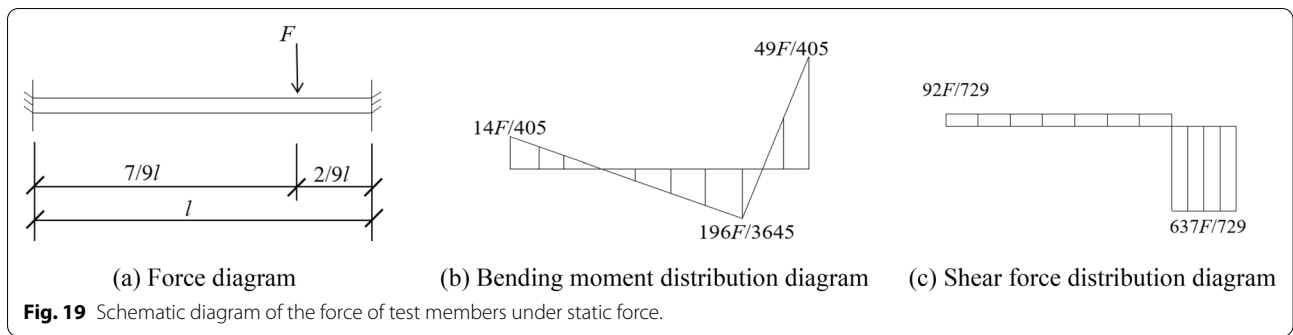


Fig. 18 Impact load from load cell within the hammer with impact duration on specimens.

(see Sect. 3.1). As stated before, both decreased specimen stiffness and increased plastic deformation result in increased impact duration.



5 Static Bending and Shear Strength

It can be shown that the specimen failure mechanism and the oblique shear crack extension range are related to the specimen stress distribution. To compute the section's ultimate bearing capacity and stress under static load, assess the member's failure mechanism under dynamic load and the relationship between shear crack type and static bearing capacity. Studies of failure pattern and cross-sectional bending and shearing strength under static load calculate the "Code for Design of Concrete Structures" sections flexural and shear bearing capacity (GB 50010-2010) (National Standard of the People's Republic of China, 2010). The section's shear strength is calculated as follows:

$$M \leq \frac{2}{3} \alpha_1 f_c A r \frac{\sin \pi \alpha + \sin \pi \alpha_t}{\pi} + f_y A_s r_s \frac{\sin \pi \alpha + \sin \pi \alpha_t}{\pi}, \tag{3}$$

where α_1 is a coefficient related to concrete strength grade; $C50 \Rightarrow \alpha_1 = 1.0$; f_c is the axial compressive strength of concrete; A is the area of the circular section; r is the radius of the circular section; α is the ratio of central angle cross-sectional area in the compression zone; f_y is the yield strength of the steel bar; A_s is the cross-sectional area of longitudinal steel bars; r_s is the radius of the circumference of the longitudinal steel bar's center of gravity; $\alpha_t = 1.25 - 2\alpha$ is the ratio of the cross-section area for the longitudinally tensioned steel bar to longitudinal steel bar. Following the section shear strength calculation, the rectangular section shear strength formula is applied. A rectangular section's shear strength is calculated as follows:

$$V \leq \frac{1.75}{\lambda + 1} f_t b h_o + f_y v \frac{A_{SV}}{S} h_o, \tag{4}$$

where $\lambda = \frac{a}{h_o}$; h_o is the effective height of the cross-section; f_t is the axial concrete tensile strength; b is the rectangular section width; A_{SV} is the total cross-sectional area of each stirrup leg.

The specimen's two fixed supports ends are 900 mm apart, and the impact site is 200 mm from the right end

Table 6 Static bearing capacity of specimens.

Specimen no.	M (kN m)	V (kN)	P_{usc} (kN)	V_{usc} (kN)
YH1	2.68	37.58	22.18	43.00
YH2	2.68	37.58	22.18	43.00
YH3	5.62	37.58	46.43	43.00
YH4	2.68	25.69	22.18	29.36

support. The specimen's internal force diagram is determined using the static method Fig. 19a. On the right end support, the maximum bending moment is illustrated in Fig. 19b. As the bending moment decreases, this part is considered harmful. The member's static bending moment resistance is estimated based on the maximum external load resistance of the critical section. According to the experimental findings, the maximum shear section of the member is placed on the right side of the impact point (Fig. 19c). Oblique cracks formed on the right side of the impact point and split. The critical section makes a similar calculation of the member's shear force to determine its static shear resistance.

Table 6 shows the results of the calculations, where P_{usc} denotes static bending moment resistance and V_{usc} denotes static shear resistance.

6 Conclusion

The behavior of RC concrete specimens under unequal lateral impact loads is investigated. The study's conclusions are summarized below:

1. An unequal high-speed impact causes shear failure. The impact point is at the top end of the failing surface, and the right side creates shear failure. Due to the lower end position, the impact energy, reinforcement ratio, and stirrup ratio fluctuate. Type I oblique fractures develop faster than type II oblique cracks.
2. Four specimens developed vertical cracks of varying degrees at the other bearing side. Crack growth

is related to impact energy, reinforcement ratio, and stirrup ratio. The damage range and severity increase with the impact of the test specimen. Increasing the test specimen reinforcement ratio reduces the damage range and reduces damage. The damage range of the specimen hardly increases when the stirrup ratio is increased; therefore, the effect is minimal.

3. It can be inferred from the experiment that the angle of the shear crack is related to the stiffness of the specimen and the impact velocity the specimen bears. It seems that all RC specimen's failure modes have undergone devastating shear failure. The specimen is crashed to eliminate the concrete fragments' form.
4. Increasing the impact energy by increasing impact height increases the peak impact force but not the plateau value. The reinforcement ratio has a minor effect on peak impact force, but it may significantly raise plateau value. Enlarging the stirrups ratio may significantly increase the specimen energy consumption capacity.
5. Both initial and final displacement increase practically linearly with increasing impact energy. The reinforcing and stirrup ratios may be increased to decrease the displacement increment at the impact force plateaus. Changes in the stirrup ratio have a significant influence on the final displacement.
6. Increasing longitudinal reinforcement influences strain capacity in preventing punching shear fractures in concrete members. In addition, decreasing the stirrup ratio makes the strain values lower.
7. Unequal impact loading increases impact duration except in failure situations. Impact duration increases with specimen stiffness and plastic deformation.
8. The critical section calculates the member's static shear resistance using the shear force. Oblique cracks and splits are produced on the right side of the impact point. The member's static bending moment resistance is determined using the critical section's greatest external load resistance.

7 Further Research

It is essential to examine the specimens' response to axial force. Attempts should be made to identify feasible approaches to enhance the ability value associated with FRP sheet wrapping in reinforcement concrete. In the construction sector, the outcomes of such investigations would be of immediate assistance.

Acknowledgements

The authors would like to express many thanks to the authority of the National Natural Science Foundation of China (Grant Nos. 52178168 and 51378427) for

financing this research work and several ongoing research projects related to the structural impact performance.

Author contributions

All authors read and approved the final manuscript.

Authors' information

Khalil AL-Bukhaiti, Ph.D. Candidate, Email: eng.khalil670@hotmail.com (first and corresponding author), Research Fellow at School of Civil Engineering, Southwest Jiaotong University, Chengdu, Sichuan, 610031, China. Liu Yanhui, Assistance Professor, Email: yhli@swjtu.edu.cn (corresponding author), Lecturer at School of Civil Engineering, Southwest Jiaotong University, Chengdu, Sichuan, 610031, China. Zhao Shichun, Associate Professor, Email: zscswjtu@home.swjtu.edu.cn, Professor at School of Civil Engineering, Dean of School of Civil Engineering, Southwest Jiaotong University, Chengdu, Sichuan, 610031, China. Hussein Abas, Ph.D. Candidate, Email: hus670eng@gmail.com, Research Fellow at School of Civil Engineering, Southwest Jiaotong University, Chengdu, Sichuan, 610031, China. Xu Nan, Email: nx@my.swjtu.edu.cn, Master student at School of Civil Engineering, Southwest Jiaotong University, Chengdu, Sichuan, 610031, China. Yang Lang, Email: yang@my.swjtu.edu.cn, Master student at School of Civil Engineering, Southwest Jiaotong University, Chengdu, Sichuan, 610031, China. Yan Xing Yu, Email: yanx@my.swjtu.edu.cn, Master student at School of Civil Engineering, Southwest Jiaotong University, Chengdu, Sichuan, 610031, China. Han Daguang, Assistance Professor, Email: daguang@oslomet.no, Lecturer at Department of Civil Engineering and Energy Technology Faculty of Technology, Art and Design Oslo Metropolitan University, Oslo, 0985, Norway.

Data availability

The datasets used and analyzed during the current study are available from the corresponding author upon reasonable request.

Declarations

Competing interests

The authors declare that they have no competing interests.

Author details

¹School of Civil Engineering, Southwest Jiaotong University, Chengdu, China. ²Department of Civil Engineering and Energy Technology, Art and Design, Oslo Metropolitan University, Oslo, Norway.

Received: 18 November 2021 Accepted: 15 April 2022

Published online: 21 July 2022

References

- AL-Bukhaiti, K., Yanhui, L., Shichun, Z., Abas, H., & Aoran, D. (2021). Dynamic equilibrium of CFRP-RC Square elements under unequal lateral impact. *Materials*, *14*, 3591. <https://doi.org/10.3390/MA14133591>
- Alharbi, Y. R., Galal, M., Abadel, A. A., & Kohail, M. (2021). Bond behavior between concrete and steel rebars for stressed elements. *Ain Shams Eng. J.*, *12*, 1231–1239. <https://doi.org/10.1016/J.ASEJ.2020.10.001>
- Anil, Ö., Tuğrul Erdem, R., & Tokgöz, M. N. (2018). Investigation of lateral impact behavior of RC columns. *Computers and Concrete*, *22*, 123–132. <https://doi.org/10.12989/cac.2018.22.1.123>
- Bhatti, A. Q., Kishi, N., & Mikami, H. (2011). An applicability of dynamic response analysis of shear-failure type RC beams with lightweight aggregate concrete under falling-weight impact loading. *Materials and Structures* *44*, 221–231. <https://doi.org/10.1617/S11527-010-9621-9>
- Bischoff, P. H., Perry, S. H., & Eibl, J. (1990). Contact force calculations with a simple spring-mass model for hard impact: A case study using polystyrene aggregate concrete. *International Journal of Impact Engineering*, *9*, 317–325. [https://doi.org/10.1016/0734-743X\(90\)90005-G](https://doi.org/10.1016/0734-743X(90)90005-G)
- Cai, J., Bin Ye, J., Chen, Q. J., Liu, X., & Wang, Y. Q. (2018). Dynamic behaviour of axially-loaded RC columns under horizontal impact loading. *Engineering Structures*, *168*, 684–697. <https://doi.org/10.1016/J.ENGSTRUCT.2018.04.095>

- Chen, Z., Fang, H., Zhu, L., Mao, Y., & Liu, W. (2020). Experimental tests and numerical simulations of circular reinforced concrete piers under ship impact. *Advances in Bridge Engineering*, 1, 1–25. <https://doi.org/10.1186/S43251-020-00002-X>
- Daudeville, L., & Malécot, Y. (2011). Concrete structures under impact. *European Journal of Environmental and Civil Engineering*, 15, 101–140. <https://doi.org/10.1080/19648189.2011.9695306>
- Do, T. V., Pham, T. M., & Hao, H. (2019). Impact force profile and failure classification of reinforced concrete bridge columns against vehicle impact. *Engineering Structures*, 183, 443–458. <https://doi.org/10.1016/J.ENGSTRUC.2019.01.040>
- Dok, G., Caglar, N., Ilki, A., & Yilmaz, C. (2021). Residual load bearing capacity and failure mechanism of impacted high-strength reinforced concrete shear beams. *Engineering Failure Analysis*, 121, 105185. <https://doi.org/10.1016/J.ENGFAILANAL.2020.105185>
- Fujikake, K., Li, B., & Soeun, S. (2009). Impact response of reinforced concrete beam and its analytical evaluation. *Journal of the Structural Engineering. American Society of Civil Engineers*, 135, 938–950. [https://doi.org/10.1061/\(ASCE\)ST.1943-541X.0000039](https://doi.org/10.1061/(ASCE)ST.1943-541X.0000039)
- GB/T 228.1–2010: Translated English of Chinese Standard, n.d. Retrieved January 28, 2020 from https://books.google.co.il/books/about/GB_T_228_1_2010_Translated_English_of_Ch.html?id=7xd7DQAAQBAJ&redir_esc=y.
- Heng, K., Li, R., Li, Z., & Wu, H. (2021). Dynamic responses of highway bridge subjected to heavy truck impact. *Engineering Structures*, 232, 111828. <https://doi.org/10.1016/J.ENGSTRUCT.2020.111828>
- Hou, L., Peng, Y., & Sun, D. (2020). Dynamic analysis of railway vehicle derailment mechanism in train-to-train collision accidents. *Proceedings of the Institution of Mechanical Engineers, Part F: Journal of Rail and Rapid Transit*, 235, 1022–1034. <https://doi.org/10.1177/0954409720959870>
- Huo, J., Li, Z., Zhao, L., Liu, J., & Xiao, Y. (2018). Dynamic behavior of carbon fiber-reinforced polymer-strengthened reinforced concrete beams without stirrups under impact loading. *ACI Structural Journal*, 115, 775–787. <https://doi.org/10.14359/51701283>
- Icten, B. M., Atas, C., Aktas, M., & Karakuzu, R. (2009). Low temperature effect on impact response of quasi-isotropic glass/epoxy laminated plates. *Composite Structures*, 91, 318–323. <https://doi.org/10.1016/J.COMPSTRUCT.2009.05.010>
- Isaac, P. (2014). Effects of extreme impulsive loads on RC structures with a view to strengthening.
- Jia, P. C., Wu, H., Wang, R., & Fang, Q. (2021). Dynamic responses of reinforced ultra-high performance concrete members under low-velocity lateral impact. *International Journal of Impact Engineering*, 150, 103818. <https://doi.org/10.1016/J.IJIMPENG.2021.103818>
- Kang, X. J., Liu, Y. H., Zhao, L., Yu, Z. X., Zhao, S. C., & Tang, H. (2019). Dynamic response analysis method for the peak value stage of concrete-filled steel tube beams under lateral impact. *Advanced Steel Construction*, 15, 329–337. <https://doi.org/10.18057/IJASC.2019.15.4.4>
- Kishi, N., & Mikami, H. (2012). Empirical formulas for designing reinforced concrete beams under impact loading. *ACI Structural Journal* 109, 509–519. <https://doi.org/10.14359/51683870>
- Kishi, N., Mikami, H., Matsuoka, K. G., & Ando, T. (2002). Impact behavior of shear-failure-type RC beams without shear rebar. *International Journal of Impact Engineering*. [https://doi.org/10.1016/S0734-743X\(01\)00149-X](https://doi.org/10.1016/S0734-743X(01)00149-X)
- Liu, Y., Al-Bukhaiti, K., Abas, H., & Shichun, Z. (2020). Effect of CFRP shear strengthening on the flexural performance of the RC specimen under unequal impact loading. *Advances in Materials Science and Engineering*, 2020, 1–18. <https://doi.org/10.1155/2020/5403835>
- Liu, Y., Dong, A., Zhao, S., Zeng, Y., & Wang, Z. (2021). The effect of CFRP-shear strengthening on existing circular RC columns under impact loads. *Construction and Building Materials*, 302, 124185. <https://doi.org/10.1016/J.CONBUILDMAT.2021.124185>
- Liu, B., Fan, W., Guo, W., Chen, B., & Liu, R. (2017). Experimental investigation and improved FE modeling of axially-loaded circular RC columns under lateral impact loading. *Engineering Structures*. <https://doi.org/10.1016/J.ENGSTRUC.2017.09.009>
- Liu, T., & Xiao, Y. (2017). Impact behavior of CFRP-strip-wrapped RC beams without stirrups. *Journal of Composites for Construction*, 21, 04017035. [https://doi.org/10.1061/\(asce\)cc.1943-5614.0000815](https://doi.org/10.1061/(asce)cc.1943-5614.0000815)
- Mylrea, T. D. (1939). Effects of impact on reinforced concrete beams. Highw. Res. Board Proc. 18.
- National Standard of the People's Republic of China, Code for Design of Concrete Structures GB 50010–2010, The Ministry of Housing and Urban-rural Development (MOHUD) and the General Administration of Quality Supervision, Inspection and Quarantine (AQSIQ) of the People's Republic of China, 2010. <https://pdfcoffee.com/gb-50010-2010-en-pdf-free.html> (accessed November 10, 2021).
- Pham, T. M., & Hao, H. (2016a). Prediction of the impact force on reinforced concrete beams from a drop weight. *Advances in Structural Engineering*, 19, 1710–1722. <https://doi.org/10.1177/1369433216649384>
- Pham, T. M., & Hao, H. (2016b). Impact behavior of FRP-strengthened RC beams without stirrups. *Journal of Composites for Construction*, 20, 04016011. [https://doi.org/10.1061/\(ASCE\)CC.1943-5614.0000671](https://doi.org/10.1061/(ASCE)CC.1943-5614.0000671)
- Roy, S., Unobe, I., & Sorensen, A. D. (2021). Vehicle-impact damage of reinforced concrete bridge piers: a state-of-the art review. *Journal of Performance of Constructed Facilities*, 35, 03121001. [https://doi.org/10.1061/\(ASCE\)CF.1943-5509.0001613](https://doi.org/10.1061/(ASCE)CF.1943-5509.0001613)
- Saatci, S., & Vecchio, F. J. (2009). Effects of shear mechanisms on impact behavior of reinforced concrete beams. *ACI Structural Journal*, 106, 78–86. <https://doi.org/10.14359/56286>
- Sha, Y., Amdahl, J., & Dørum, C. (2021). Numerical and analytical studies of ship deckhouse impact with steel and RC bridge girders. *Engineering Structures*, 234, 111868. <https://doi.org/10.1016/J.ENGSTRUCT.2021.111868>
- Tran, T. T., Pham, T. M., Huang, Z., Chen, W., Hao, H., & Elchalakani, M. (2021). Impact response of fibre reinforced geopolymer concrete beams with BFRP bars and stirrups. *Engineering Structures*, 231, 111785. <https://doi.org/10.1016/J.ENGSTRUCT.2020.111785>
- Wang, H., Huo, J., Liu, Y., Elchalakani, M., & Zhu, Z. (2021). Dynamic performance of composite beam-column connections subjected to impact loadings. *Journal of Constructional Steel Research*, 178, 106498. <https://doi.org/10.1016/J.JCSR.2020.106498>
- Wang, P., Shi, Q., Wang, F., Wang, Q., Wang, P., Shi, Q., Wang, F., & Wang, Q. (2020). Seismic behaviour of concrete columns with high-strength stirrups. *Earthquakes Struct.*, 18, 015. <https://doi.org/10.12989/EAS.2020.18.1.015>
- Wongmatar, P., Hansapinyo, C., Vimonsatit, V., & Chen, W. (2018). Recommendations for designing reinforced concrete beams against low velocity impact loads. *International Journal of Structural Stability and Dynamics*. <https://doi.org/10.1142/S0219455418501043>
- Xia, C., Ma, Q., Liao, Z., Xia, H. (2018). Numerical simulation of ship collision on RC Cap with anti-collision steel box barrier of over-sea bridge.
- Xu, B., & Zeng X. (2014). Experimental study on the behaviors of reinforced concrete beams under impact loading. *China Civ Eng. J.* 41–61.
- Xu, B., & Zeng, X. (2014). Experimental study on the behaviors of reinforced concrete beams under impact loadings. *Tumu Gongcheng Xuebao/china Civil Engineering Journal*, 47, 41–61.
- Yanhui L., AL-Bukhaiti, K, Shichun, Z., Abas, H., Zaidi, K., Xu N., Aoran D. (2022). Comparative Study on Dynamic Response of Square Section RC-Members and CFRP-Reinforced Members Under Unequal Transverse Impact Loading. https://doi.org/10.1007/978-981-16-6932-3_12.
- Yao, S. J., Zhang, D., Lu, F. Y., Wang, W., & Chen, X. G. (2016). Damage features and dynamic response of RC beams under blast. *Engineering Failure Analysis*. <https://doi.org/10.1016/J.ENGFAILANAL.2015.12.001>
- Yi, W. J., Zhao, D. B., & Kunnath, S. K. (2016). Simplified approach for assessing shear resistance of reinforced concrete beams under impact load, *ACI Structural Journal*.
- Zeinoddini, M., Parke, G. A. R., & Harding, J. E. (2002). Axially pre-loaded steel tubes subjected to lateral impacts: An experimental study. *International Journal of Impact Engineering*, 27, 669–690. [https://doi.org/10.1016/S0734-743X\(01\)00157-9](https://doi.org/10.1016/S0734-743X(01)00157-9)
- Zhan, T., Wang, Z., & Ning, J. (2015). Failure behaviors of reinforced concrete beams subjected to high impact loading. *Engineering Failure Analysis*, 56, 233–243. <https://doi.org/10.1016/J.ENGFAILANAL.2015.02.006>
- Zhang, T., Guo, X., Jin, T., Yang, Y., Ling, L., Wang, K., & Zhai, W. (2021). Dynamic derailment behaviour of urban tram subjected to lateral collision. *International Journal of Rail Transportation*. <https://doi.org/10.1080/23248378.2021.1964392>
- Zhao, D.-B., Yi, W.-J., & Kunnath, S. K. (2017). Shear mechanisms in reinforced concrete beams under impact loading. *Journal of the Structural Engineering. American Society of Civil Engineers*, 143, 04017089. [https://doi.org/10.1061/\(ASCE\)ST.1943-541X.0001818](https://doi.org/10.1061/(ASCE)ST.1943-541X.0001818)
- Zhao, W., Qian, J., & Jia, P. (2019b). Peak response prediction for rc beams under impact loading. *Shock and Vibration*. <https://doi.org/10.1155/2019/6813693>

- Zhao, W., Qian, J., & Zhang, W. (2019a). Performance and damage evaluation of RC beams under impact loading. *Baozha Yu Chongji/explosion Shock Waves*, 39, 015102–015111. <https://doi.org/10.11883/bzycj-2017-0288>
- Zhao, W., Ye, J., & Qian, J. (2021). Dynamic behavior and damage mechanisms of reinforced concrete piers subjected to truck impact. *Engineering Failure Analysis*, 121, 105158. <https://doi.org/10.1016/J.ENGFANAL.2020.105158>
- Zhu, X., Zhao, P., Tian, Y., & Wang, R. (2021). Experimental study of RC columns and composite columns under low-velocity impact. *Thin-Walled Struct.*, 160, 107374. <https://doi.org/10.1016/J.TWS.2020.107374>

Publisher's Note

Springer Nature remains neutral with regard to jurisdictional claims in published maps and institutional affiliations.

Submit your manuscript to a SpringerOpen[®] journal and benefit from:

- ▶ Convenient online submission
- ▶ Rigorous peer review
- ▶ Open access: articles freely available online
- ▶ High visibility within the field
- ▶ Retaining the copyright to your article

Submit your next manuscript at ▶ [springeropen.com](https://www.springeropen.com)
